LASER & PHOTONICS REVIEWS
www.lpr-journal.org

Machine Learning for Engineering Meta-Atoms with Tailored Multipolar Resonances

*Wenhao Li, Hooman Barati Sedeh, Dmitrii Tsvetkov, Willie J. Padilla, Simiao Ren, Jordan Malof, and Natalia M. Litchinitser**

In the rapidly developing field of nanophotonics, machine learning (ML) methods facilitate the multi-parameter optimization processes and serve as a valuable technique in tackling inverse design challenges by predicting nanostructure designs that satisfy specific optical property criteria. However, while considerable efforts have been devoted to applying ML for designing the overall spectral response of photonic nanostructures, often without elucidating the underlying physical mechanisms, physics-based models remain largely unexplored. Here, physics-empowered forward and inverse ML models to design dielectric meta-atoms with controlled multipolar responses are introduced. By utilizing the multipole expansion theory, the forward model efficiently predicts the scattering response of meta-atoms with diverse shapes and the inverse model designs meta-atoms that possess the desired multipole resonances. Implementing the inverse design model, uniquely shaped meta-atoms with enhanced higher-order magnetic resonances and those supporting a super-scattering regime of light-matter interactions resulting in nearly five-fold enhancement of scattering beyond the single-channel limit are designed. Finally, an ML model to predict the wavelength-dependent electric field distribution inside and near the meta-atom is developed. The proposed ML based models will likely facilitate uncovering new regimes of linear and nonlinear light-matter interaction at the nanoscale as well as a versatile toolkit for nanophotonic design.

1. Introduction

Rapid progress in photonics and nanofabrication has opened up new prospects for realizing engineered structures to manipulate light at the nanoscale.[1] These subwavelength scatterers can be arranged in isolated, 2 and 3D arrangements, known as meta-atoms,[2] metasurfaces,[3] and metamaterials,[4] respectively, and have been shown to facilitate various applications such as beam steering,[5] holography,[6] nonlinear harmonic generation,[7] and Kerker, anti-Kerker, and transverse Kerker effects,[8] to name a few. While electromagnetic multipole expansion theory, a cornerstone of light-matter interactions, has facilitated the study of these remarkable optical phenomena, brute force optimization methods relying on an iterative exploration of various geometries and materials are conventionally employed to obtain the desired response.[9–13] However, these approaches are computationally demanding and less effective for intricate designs, which leads to a fundamental trade-off between performance and time, emphasizing the need for alternative methods that offer faster and more efficient solutions to overcome these limitations.

In recent years, the maturation of machine learning (ML) models has led to numerous breakthroughs in various domains, including finance,[14] healthcare,[15] computer vision,[16] and robotics.[17] Following this significant progress in other fields of research and technology, ML has recently emerged as a powerful tool in photonics for the optimization and analysis of various subwavelength structures and systems.[18–33] In particular, contrary to the conventional numerical approaches, ML methods offer fast prediction techniques that facilitate the optimization process within a multi-parameter space and serve as a valuable technique in tackling inverse design challenges by predicting nanostructure geometries that satisfy specific optical property criteria. Although considerable effort has been devoted to applying ML for designing the overall spectral response of optical metasurfaces, often without elucidating the underlying physical mechanisms,[34–40] only a few studies of the resonant response of meta-atoms in terms of their multipoles (or cavity modes) as well as the electromagnetic field distributions inside the meta-atoms using ML has been reported. In this context, Wiecha et al.[41] recently demonstrated the feasibility of predicting electromagnetic field distributions within subwavelength meta-atoms at fixed wavelengths. Other recent studies

W. Li, H. Barati Sedeh, D. Tsvetkov, W. J. Padilla, S. Ren, N. M. Litchinitser
Department of Electrical and Computer Engineering
Duke University
Durham, NC 27708, USA
E-mail: natalia.litchinitser@duke.edu
J. Malof
Department of Computer Science
University of Montana
Missoula, MT 59812, USA

The ORCID identification number(s) for the author(s) of this article can be found under https://doi.org/10.1002/lpor.202300855

DOI: 10.1002/lpor.202300855

employed ML and optimization techniques for meta-atom design primarily involving regular and relatively simple geometries such as spheres,[42] core–shell structures,[43–46] cubes,[47] and cylinders,[48] which typically support only low-order multipolar resonances. However, if ML could be applied to design the multipolar response itself by optimizing the shape of the individual meta-atoms, it may facilitate entirely new regimes of light-matter interactions relying on higher-order electric and magnetic multipolar resonances that have been largely neglected to date. Judicious design of such higher-order resonances is likely to enable high confinement and large mode overlap of electromagnetic fields at different frequencies essential for enhancing nonlinear frequency conversion efficiency[49–55] or establishing strong coupling in 2D materials.[56–58]

Here, we apply ML to design dielectric meta-atoms supporting desired multipolar moments as schematically illustrated in **Figure 1**. In particular, we use multipole expansion theory to expand electromagnetic fields on a multipolar basis and establish a connection between the induced electromagnetic fields and the topological features of meta-atoms.[9–13] To the best of our knowledge, this is the first time ML has been employed in this context. We demonstrate the effectiveness of the ML approach in generating uniquely shaped meta-atoms with tailored resonances by developing forward prediction models (FPM) to establish the relationships between scattering response and topological attributes of individual meta-atoms (shown in the blue box in Figure 1) and an inverse design model (IDM) to retrieve the meta-atoms with desired multipolar moments (orange box). To address the unique challenges of inverse modeling, we employ a specialized deep learning architecture, termed the Tandem model, which we use to maximize a particular multipolar moment. We demonstrate the effectiveness of the proposed approach with two examples. First, we design meta-atoms supporting higher-order magnetic dipole and octupole resonant modes contributing 60% to the optical response. Next, we optimize meta-atoms for establishing a super-scattering regime of light-matter interactions, with nearly a five-fold scattering enhancement beyond the single-channel limit. Additionally, we developed an ML model to predict the wavelength-dependent electric field distribution inside and near the meta-atom (green box in Figure 1). The developed approach can be readily applied to existing datasets and integrated with various network architectures and problem domains, making it a valuable tool in nanophotonics.

1.1. Forward Prediction Model

The induced polarization due to the interaction of light with a meta-atom is related to the field distribution inside the meta-atom through $\boldsymbol{P} = \epsilon_0\ (\epsilon_p - \epsilon_d)\boldsymbol{E}_p$, where ϵ_0, ϵ_p and ϵ_d are the dielectric permittivities of free space, the meta-atom, and the surrounding medium, respectively, and $\boldsymbol{E}_p$ is the total electric field within the meta-atom.[9–13] Since induced polarization can be described in terms of induced multipoles, the availability of an efficient tool for designing such multipoles with specific magnitudes at a given wavelength is essential. However, computing multipole moments using conventional numerical methods such as the finite elements method (FEM) can be time-consuming, particularly for complex structures. Therefore, here we develop an ML approach as an efficient alternative and develop an FPM capable of approximating multipolar resonances based on the shape of a meta-atom in the target spectral range of 500–900 nm. The FPM employs a densely connected convolutional network (DenseNet) encoder architecture,[59] which is orders of magnitude faster than conventional commercial software-based simulations. In this approach, the meta-atom shape information is compressed into a reduced dimension (bottleneck) following a series of down-conversion blocks (DCBs). This condensed information and the associated wavelength are then passed through fully connected dense layers to predict the multipolar resonances at a given wavelength, as shown in **Figure 2a**.

A dataset of 36 300 distinct combinations of titanium dioxide (TiO_2) meta-atom shapes and wavelengths were used to train and validate the ML model. The height of meta-atoms was fixed to 320 nm, while their geometrical cross-sections in the transverse plane were varied as a function of azimuthal angle (see Supporting Information for more details). First, numerical simulations using the FEM implemented in COMSOL Multiphysics have been performed at 21 discrete points within the spectral window of interest to calculate the electric field distribution and the induced multipoles corresponding to various TiO_2 meta-atoms geometries. Contrary to most prior studies, which primarily consider the first four multipole moments to characterize the optical response of regular-shaped optical meta-atoms,[41–48] we take into account higher-order multipoles up to the magnetic octupole term (see Experimental Section for details). While lower-order multipoles dominate in the scattering cross-section of the regularly shaped meta-atoms such as cylinders or cubes, higher-order moments become important in the case of irregularly shaped meta-atoms. Figure 2b shows the scattering cross-section of a particular TiO_2 meta-atom that was used in training the ML model (shape (ii) in panel (a)) across the spectral range of 500–900 nm. As can be seen, the spectral response of the meta-atom at various wavelengths is predominantly governed by distinct types of moments. Specifically, its response can be primarily attributed to the electric and magnetic dipoles at longer wavelengths, while contributions from higher-order moments become increasingly evident at shorter wavelengths. The emergence of higher-order moments at shorter wavelengths can be ascribed to the meta-atom size in this region being comparable with the operating wavelength. Comparing the total scattering response of the meta-atom and the response derived from the summation of the first six multipoles, including electric and magnetic dipoles, electric (ED, MD) and magnetic quadrupoles (EQ, MQ), and electric and magnetic octupoles (EO, MO), justifies the sufficiency of considering the first six multipole moments and neglecting the multipolar terms higher than MO.

We have also compared the results obtained from the multipole expansion with those derived from Mie theory for the light scattered by spherical particles (see Supporting Information for more details of this comparative analysis). Figure 2c demonstrates the average values, their corresponding standard deviations, and types of resonant modes supported by the training dataset. At longer wavelengths, the major contribution to the overall dataset comes from the low-order ED and MD moments, whereas at shorter wavelengths, higher-order moments such as MO, are emerging. The performance of the predictive model is

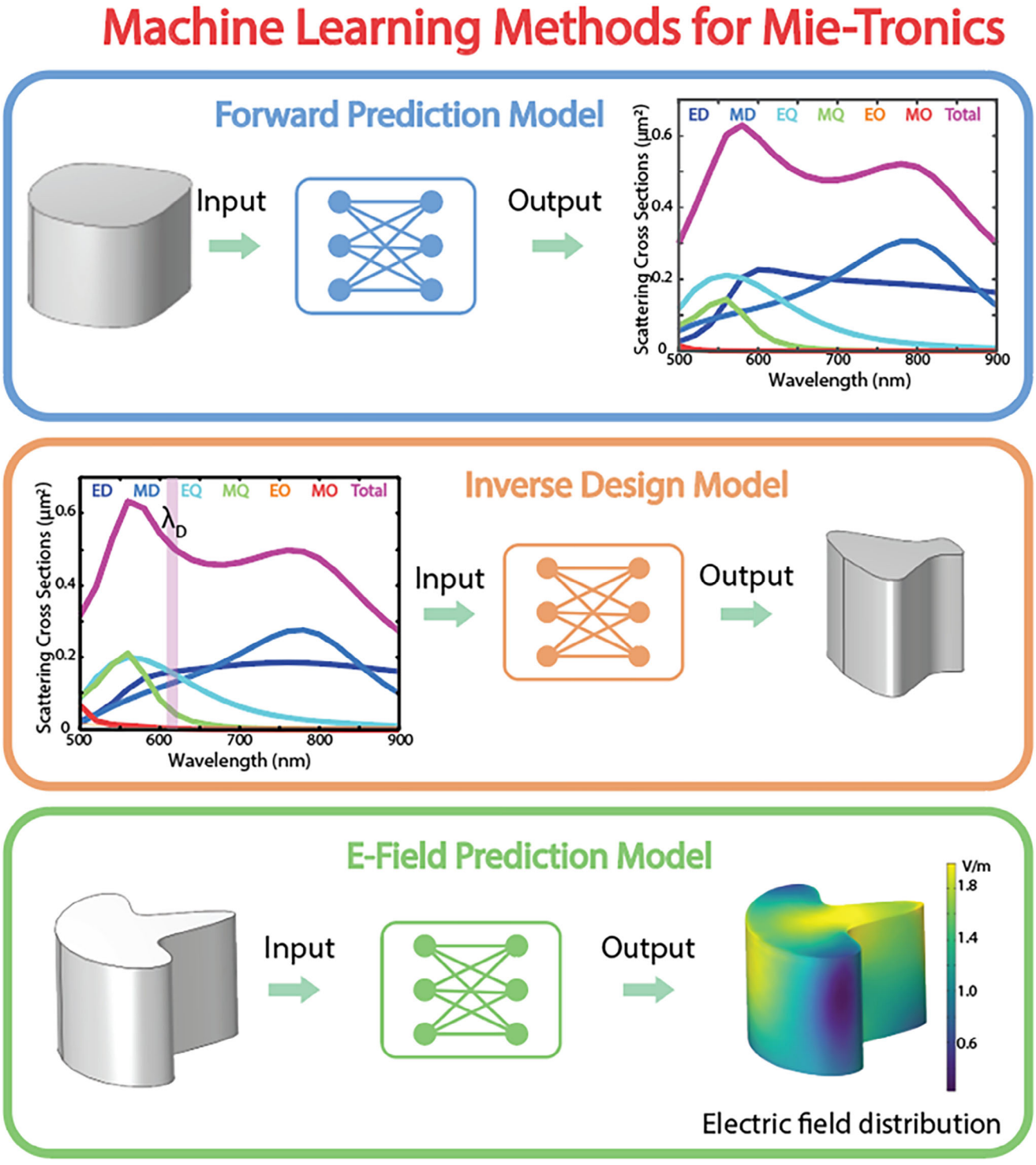

Figure 1. Schematic illustration of the concept of ML for Mie-Tronics. In the FPM, shown in the blue box, the meta-atom geometry serves as the input, allowing the model to predict its optical response in terms of multipole moments up to the magnetic octupole. In the IDM, shown in the orange color, the model uses the magnitudes of the desired multipolar moments at a given wavelength, given by λ_D, as an input and predicts the explicit geometry that yields the specified response. The third model, shown in the green box, predicts the electric field distribution inside the meta-atom of a particular shape at the desired operating wavelength.

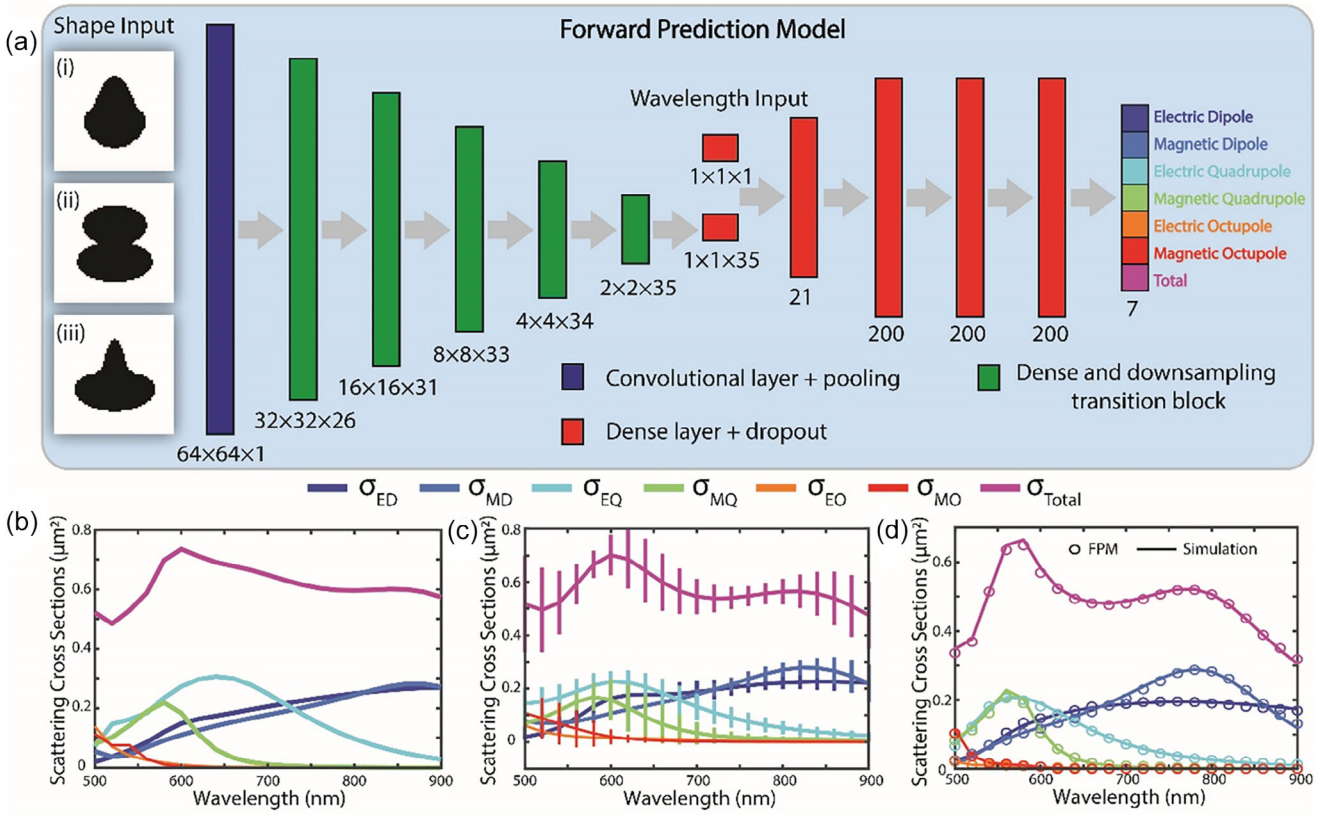

Figure 2. Predictions of the meta-atom optical response using the FPM. a) The schematic illustration of an FPM is used to predict the optical response of the input meta-atom. The shape information undergoes compression into a reduced dimension using multiple DCBs. Subsequently, this condensed information, in conjunction with wavelength information, is processed through fully connected dense layers to accurately predict multipolar resonances for a specified wavelength. b) The scattering cross-section of a single meta-atom corresponding to the shape (ii) in panel (a). c) The statistical representation of moments for the complete training dataset shown within the spectral range spanning from 500 to 900 nm. The solid lines and error bars within the graph correspond respectively to the mean and standard deviation of the specific moments. d) A comparison of the scattering cross-section between direct simulation results (solid line) and predictions from the FPM (circle marker) for an arbitrary input meta-atom (shape (iii) in panel (a)).

assessed using the root mean square error (RMSE) loss metric, which quantifies the deviation of the predicted resonance values from the actual ones. In particular, the RMSE loss for the predicted resonances in the validation dataset is calculated to be $6.4 \times 10^{-3} \mu m^2$, which is more than two orders of magnitude lower than the average value of the resonances, demonstrating the competency of the employed model to generate accurate predictions with minimal error relative to the overall resonance values (see Supporting Information for more details).

Figure 2d shows a comparison of the resonances of a meta-atom (corresponding to shape (iii) in panel (a)) obtained through direct simulation (solid line) and those predicted by FPM (circle curves) across 21 wavelengths in the spectral range of 500–900 nm. The close agreement between the simulation and FPM-predicted results illustrates the accuracy of the implemented model in predicting the response of meta-atoms.

1.2. Inverse Design Model

While the developed FPM provides a fast and accurate way of estimating the multipolar resonances for a given meta-atom, designing a meta-atom with on-demand resonances still requires searching the shapes of the meta-atoms. To simplify the designing process, an inverse design method that obtains the meta-atom corresponding to a desired multipolar response is needed. Inverse design problems are often deemed ill-posed for two main reasons: i) existence—a meta-atom with the given multipolar resonances might not exist, and ii) uniqueness—multiple meta-atoms could share highly similar multipolar resonances.[18–40] In the meta-atoms design process, our primary concern revolves around the relative strength of resonances at the intended wavelength. Therefore, we opt to use the moments specifically at the design wavelength as input rather than considering moments across the entire wavelength range. This approach helps mitigate the existence issue, but it may introduce the uniqueness challenge due to the reduced number of input elements required.

For such reasons, conventional deep learning models (e.g., a DenseNet) would not work well when applied directly to learn an inverse relationship. To overcome such an issue and avoid generating inaccurate designs due to sample non-uniqueness, we implemented a Tandem inverse design model (TIDM),[60] schematically shown in **Figure 3**a. The TIDM model was chosen because of its reliable training procedure. Also, based on a recent comparison of inverse modeling approaches, we found it to offer a useful tradeoff between accuracy and computation time.[61] In

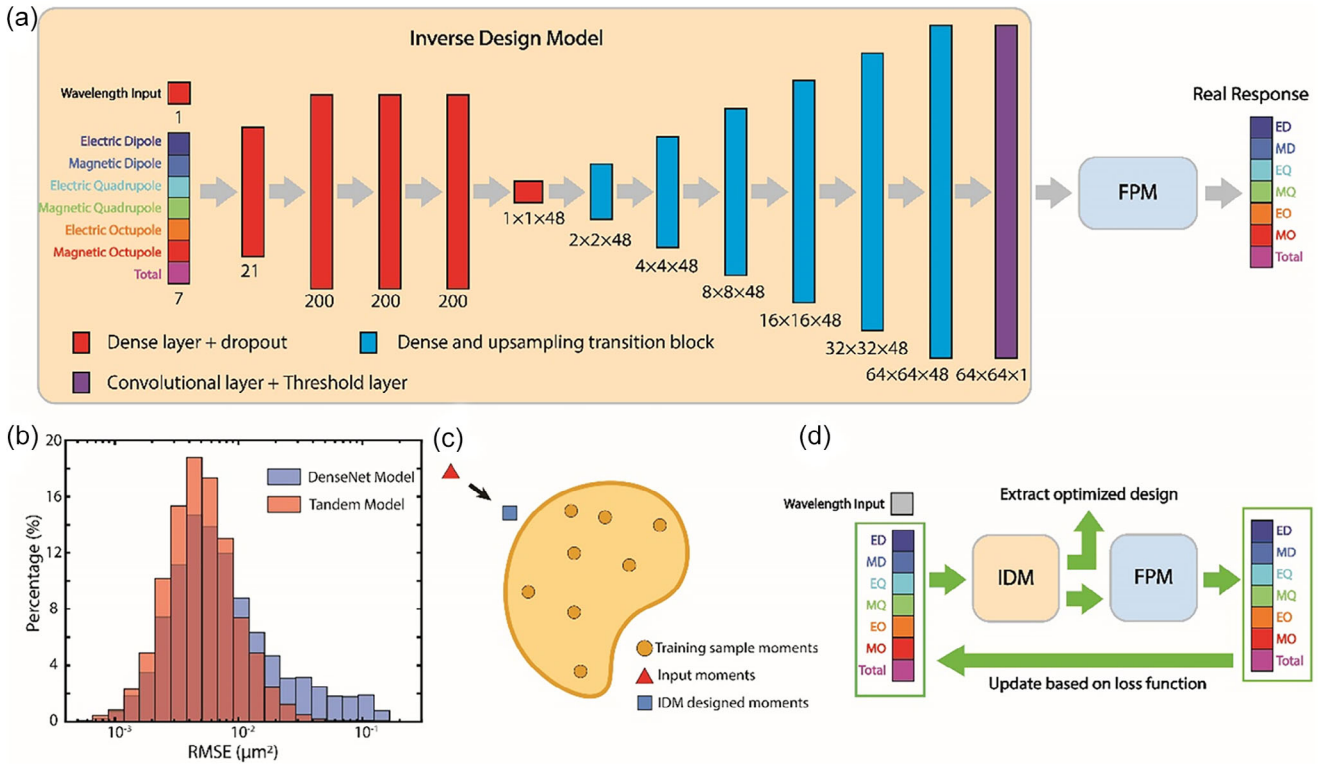

Figure 3. Meta-atom optimization using inverse design model. a) The schematic diagram of the implemented IDM used for designing meta-atom geometry based on the desired optical response at a specified operating wavelength. The MSE loss (the difference between the target response and the one predicted by the FPM) is incorporated as feedback to ensure finding an optimal solution. b) Histogram of the RMSE on validation dataset for the TIDM model and DenseNet model. c) Conceptual illustration of the approach implemented to address a potential nonexistence problem that may arise during the inverse design process. d) Illustration of the optimization-based inverse design procedure.

particular, the employed model consists of two components: a DenseNet decoder for designing meta-atom shapes and a pre-trained FPM for validating the resonances of the designed meta-atom. To ensure the design convergence, the MSE metric, which quantifies the difference between the desired resonances (i.e., target response) and the ones obtained from FPM is implemented as the feedback for updating the decoder weights while maintaining its FPM counterparts fixed. Within this configuration, the IDM is forced to select a single realization of meta-atoms capable of generating the desired resonances while ignoring alternative possibilities.

To evaluate the performance of the IDM, meta-atoms are designed using the wavelength and resonances from the validation dataset, and their resonances are predicted using FPM. Figure 3b demonstrates the histogram of the RMSE between the predicted and designed resonances using the TIDM and DenseNet models. The average RMSE from TIDM is $6.5 \times 10^{-3} \mu m^2$, which is two orders of magnitude lower than the average of the resonances, while the DenseNet model yields an RMSE of $1.4 \times 10^{-2} \mu m^2$. The superior performance of TIDM suggests that it contributes to mitigating the uniqueness problem. It should be noted that in the process of designing a meta-atom, it is inherently uncertain whether meta-atoms with specified resonances exist or not. Moreover, if such meta-atoms could be found, their shape characteristics could diverge considerably from those of the training samples, leading to an underwhelming performance of the IDM. To address this issue, we tested the performance of the IDM by providing it with input moments that significantly deviate from those in the training dataset, and it is found that the IDM tends to generate results that align closely with the training dataset examples within a specific confidence range as it is shown in Figure 3c (see Supporting Information for more details). Based on the performance of IDM for the case of non-existence, we developed an optimization-based inverse design procedure as illustrated in Figure 3d. First, the IDM provides a meta-atom design given a desired set of multipolar moments. We then propose a second inverse design step to further improve the IDM-based meta-atom design, inspired by the so-called Neural-Adjoint method from the deep learning literature.[62] Our proposed approach relies upon using the FPM to estimate the moments of the IDM-designed meta-atoms, and with this information, we can evaluate the discrepancy between the moments of our design and those that we ultimately desire. We can quantify this discrepancy using a loss function that takes the predicted moments and the desired moments as input and returns a single scalar value indicating the relative level of discrepancy between the two (i.e., higher numbers mean greater discrepancy). As long as the loss function is differentiable, it can be customized to precisely reflect the properties of the moments that we desire (e.g., acceptable loss functions include mean squared error, or mean absolute error). The loss function and the FPN together create a fully differentiable function that maps a given meta-atom design

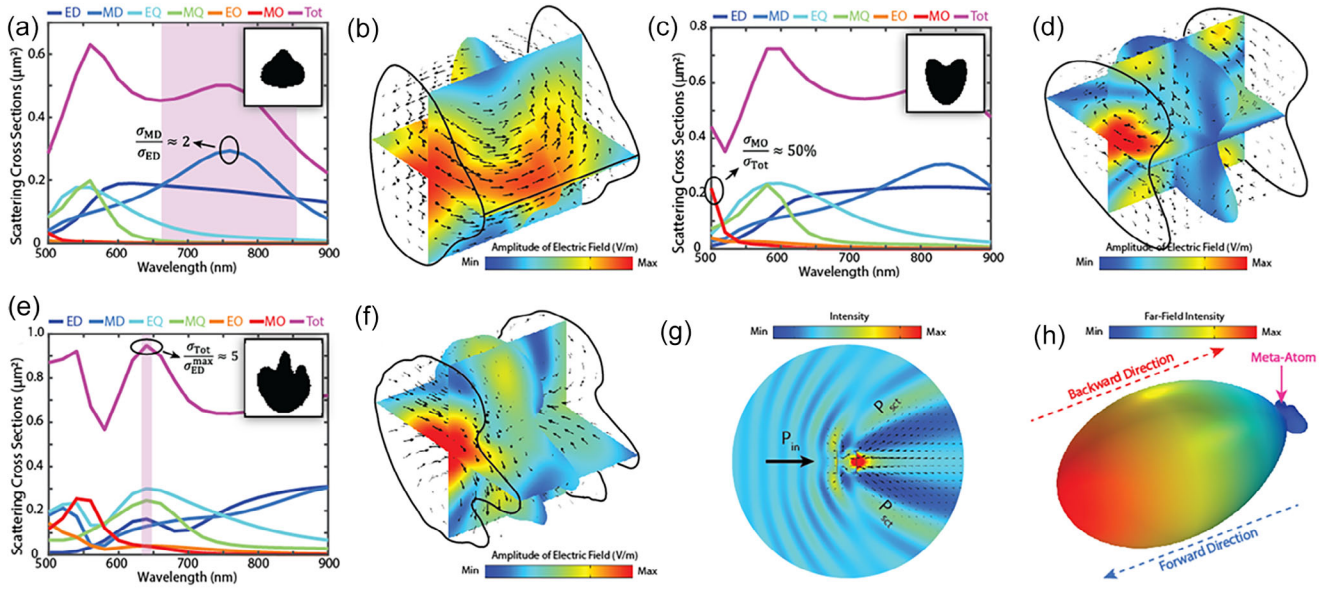

Figure 4. Engineering magnetic and super-scattering responses through IDM. The scattering spectra of the designed meta-atoms for supporting a) MD and c) MO with the contribution of 61% and 50% of the total response at the operating wavelengths of $\lambda_{MD} =$ 780 and $\lambda_{MO} =$ 500 nm, respectively. The 3D near-field distribution of the representative examples supporting b) MD and d) MO resonant modes, with black arrows representing the electric field. e) The scattering spectra of the third meta-atom, designed to support a super-scattering state at $\lambda_{SS} =$ 633 nm. A five-fold enhancement of scattering, compared to the single-channel limit ($\frac{\sigma_{Total}}{\sigma_{ED}^{max}} \approx 5$) can be observed at the designed wavelength. f) The amplitude of the electric field within the super-scatterer at $\lambda_{SS} =$ 633 nm and g) its corresponding intensity distribution in the background environment. The black arrows in panel (g) represent the relative Poynting vectors, which tend to scatter in the forward direction. h) The far-field radiation pattern of the super-scatterer at λ_{SS}. The designed meta-atom significantly scatters in the direction of the incident beam with a maximal directivity of ≈9 dB.

to its loss, and therefore we can compute the derivative of the loss with respect to the meta-atom design and use gradient descent to iteratively adjust the meta-atom design to minimize our loss, and thereby improve the quality of our meta-atom design. We demonstrated the inverse design procedure using the following examples: we engineered meta-atoms with i) dominant strong magnetic multipolar responses and ii) super-scattering.

1.3. Magnetic Octupolar Response

The realization of efficient optical magnetism using nonmagnetic nanostructures is of interest for many potential applications such as Fano resonances,[63–65] enhanced optical nonlinearity,[66] directional scattering of light,[67–70] and Purcell factor enhancements[71] to name a few. Therefore, next, we show examples of meta-atoms with the dominant contributions of magnetic resonances such as MD, MQ, and/or MO relative to other resonant modes. Although to date, various methods have been proposed to attain this particular regime of light-matter interaction, these approaches typically involve constraints in terms of geometry, such as core–shell structures,[72] or depend on the specific excitation of nonradiating states, such as optical anapolis.[73] Here we demonstrate the capability of our IDM to predict and design two different meta-atoms supporting magnetic responses (MD and MO) at two distinct operating wavelengths. To maximize the dipole and octupole magnetic responses, the loss functions for each of the representing examples are set to be $L_{MD} = -\sigma_{MD}/\sigma_{Tot}$ and $L_{MO} = -\sigma_{MO}/\sigma_{Tot}$, wherein σ_α denote the scattering cross-section of a particular resonant mode of α, being MD, MO or total in this case. These loss functions are subsequently employed to iteratively update the resonant characteristics within the input layer (i.e., the meta-atom design) until they converge to a minimum value. Once this convergence is achieved, the design of the meta-atom is extracted from the optimized parameters. Using this method, we designed a meta-atom with the MD resonance contribution of ≈61% of the total response at an operating wavelength $\lambda_{MD} =$ 780 nm as shown in **Figure 4a**. We note that at the corresponding wavelength of λ_{MD}, the contribution of MD is almost two times higher than that of the ED moment, i.e., $\sigma_{MD}/\sigma_{ED} \approx 2$, in a relatively broad bandwidth of ≈ Δ193 m. In the second example, we designed a meta-atom supporting MO moment contributing ≈50% of the total scattering cross-sections at $\lambda_{MO} =$ 500 nm, as shown in Figure 4c (see Supporting Information for more details on the optical response of the MO meta-atom in the region of 450 nm < λ < 550 nm). We note that to the best of our knowledge, achieving such a high degree of magnetic contribution, particularly for higher-order moments such as MO, has not been previously demonstrated within an isolated scatterer. In addition to the scattering cross-section spectra, Figure 4b,d show the field distribution within the meta-atoms at their respective MD and MO resonant modes' operating wavelengths, respectively.

1.4. Super-Scattering Optical Response

Achieving enhanced wave scattering from subwavelength particles is of utmost importance in various applications, including sensors, miniaturized antennas, and energy harvesting

devices.[71–76] However, the design of such scatterers is challenging owing to the inherent limitation known as the single-channel limit that establishes an upper boundary for the scattering cross-section of such meta-atoms which is bounded to $(2l+1)\lambda^2/2\pi$, wherein l represents the order of the multipole and can only be achieved under resonance conditions for a specific scattering mode or channel.[64,80,81] However, if multiple modes resonantly scatter at a particular frequency, this limit can be overcome resulting in the so-called super-scattering state. As a result, in the super-scattering regime, the total scattering cross-section surpasses the given single-channel limit of an electric dipole ($l = 1$) such that $\frac{\sigma_{\text{Tot}}}{\sigma_{\text{ED}}^{\max}} = \frac{2\pi\ \sigma_{\text{Total}}}{3\lambda^2} > 1$.[71–79] Although the initial proposal for achieving a state of super-scattering concentrated on cylindrical structures comprising multiple plasmonic and dielectric layers,[75] the experimental results revealed that the measured enhancement in wave scattering was ≈50% less than predicted (from eight times enhancement to four times) or, in some cases, even nonexistent,[82] which was attributed to the losses in the plasmonic materials. A similar phenomenon was observed in core–shell plasmonic nanowires, where the scattering cross section slightly exceeded the single-channel limit in the presence of material losses[82] and both in the terahertz and microwave frequency regimes.[83,84] To minimize the effect of losses, we employ our developed IDM to design an all-dielectric meta-atom that supports a state of super-scattering. Remarkably, our proposed structure surpasses the previously reported enhancement values while maintaining a rather simple design as compared to the multilayered structures or the utilization of metasurfaces around the meta-atom.[85] In contrast to previous studies that aimed to spectrally align the peaks of contributing moments at a single frequency, our approach focuses on directly maximizing the total scattering cross-section (i.e., σ_{Tot}) offering several advantages. First, it incorporates all potential contributions up to the MO moment, allowing for a detailed analysis of various scattering responses. Additionally, it broadens the design space since the maximum total scattering cross-section does not necessarily correspond to the case of all peaks aligned at a single frequency (which is a difficult or sometimes not feasible condition to achieve). To this end, we defined the corresponding loss function to be $L_{\text{SS}} = -\sigma_{\text{Tot}}$, which is used to update the resonant characteristics within the input layer of the ML model until the final design of the meta-atom with the optimized parameters is found. The optimized geometry shown in the inset of Figure 4e possesses a total scattering cross-section of $\sigma_{\text{Tot}} = 0.94\ \mu\text{m}^2$ (0.945 μm^2 predicted by FPM) at the operating wavelength of $\lambda_{\text{SS}} = 633$ nm. According to the obtained result, such a meta-atom operates in the super-scattering regime with the total enhancement of $\frac{\sigma_{\text{Total}}}{\sigma_{\text{ED}}^{\max}} \approx 5$, which to the best of our knowledge is the highest reported value calculated within a simple all-dielectric platform that is not reliant on the alignment of peaks from individual contributing moments, but rather on their collective overlap as shown in Figure 4e. This significant improvement in scattering arises from the maximization of the total scattering cross-section, which considers the overall contribution of each moment, rather than focusing solely on individual moments. Figure 4f,g show the near-field and intensity distributions at the corresponding wavelength of λ_{SS} within the meta-atom and its background environment, respectively. The directional scattering behavior of the designed meta-atom is evident from the components of the relative Poynting vector in panel 4(g), indicating that the meta-atom preferably scatters light in the forward direction, while the backscattering is minimized. This unidirectional scattering behavior is also reflected in the meta-atoms radiation pattern, which exhibits a high directivity, as shown in Figure 4h. The directivity of the meta-atoms has been calculated using $D = \frac{4\pi\ U(\theta,\varphi)}{\int_0^{2\pi}\int_0^{\pi} U(\theta,\varphi)\sin(\theta)d\theta d\varphi}$, wherein $U(\theta,\varphi)$ represent the radiation intensity, while θ and φ denote the elevation and azimuthal angles, respectively.[83,86] We note that while this meta-atom demonstrated the highest scattering at the stated wavelength within our dataset, we observed other meta-atoms with superior enhancements at different wavelengths. However, given the significance of the operating wavelength in design considerations, direct comparisons with meta-atoms optimized for other wavelengths would be inappropriate. In addition, to enhance scattering further, one potential strategy involves refining our training dataset to include meta-atoms supporting higher multipolar responses. As can be seen from Figure 4e, the optical response of the current meta-atom lacks dominant MO and EO resonant modes, which subsequently decreases the value of the total scattering cross-section as well as the total enhancement compared to the single channel limit. The other approach would be to include more conditions in the input such that the highest scattering response comes together with the spectral overlap of the resonant peaks rather than the mere contribution of each moment.

1.5. E-Field Prediction Model

While the FPM and IDM have been valuable in designing meta-atoms for/from far-field scattering spectra, the complete description of meta-atom scattering behavior would also benefit from understanding the electric field distribution within meta-atoms as it directly influences their scattering characteristics and is a complement to multipolar moments for applications wherein spatial overlap integral of the modes are crucial such as in nonlinear photonics.[87] In nanostructured resonant systems, the efficiency of a particular nonlinear process, such as second or third harmonic generation, depends on the spatial field overlap between the fundamental wavelength field and the harmonic field. Hence, optimizing the meta-atom shape to maximize such an overlap at the corresponding wavelengths is essential for enhancing the efficiency of the desired nonlinear process. To mitigate the computational burden associated with direct FEM-based numerical simulations of the electric field distribution, we developed a 3D electric field prediction model (EPM) capable of predicting the electric field within the given meta-atoms as shown in **Figure 5**a. In particular, the implemented model employs a 3D DenseNet architecture that takes the shape of the meta-atom and compresses it into reduced dimensions using six DCBs. The condensed information and the desired operating wavelength are then passed through three dense layers and six up-conversion blocks (UCBs) to accurately predict the electric fields within the given meta-atom. More specifically, the output layer consists of six channels, each corresponding to the real and imaginary parts of the electric field components or equivalently the electric field amplitude in each plane.

To quantify how far the predicted values of EPM are from the ones directly calculated with the COMSOL simulations, we

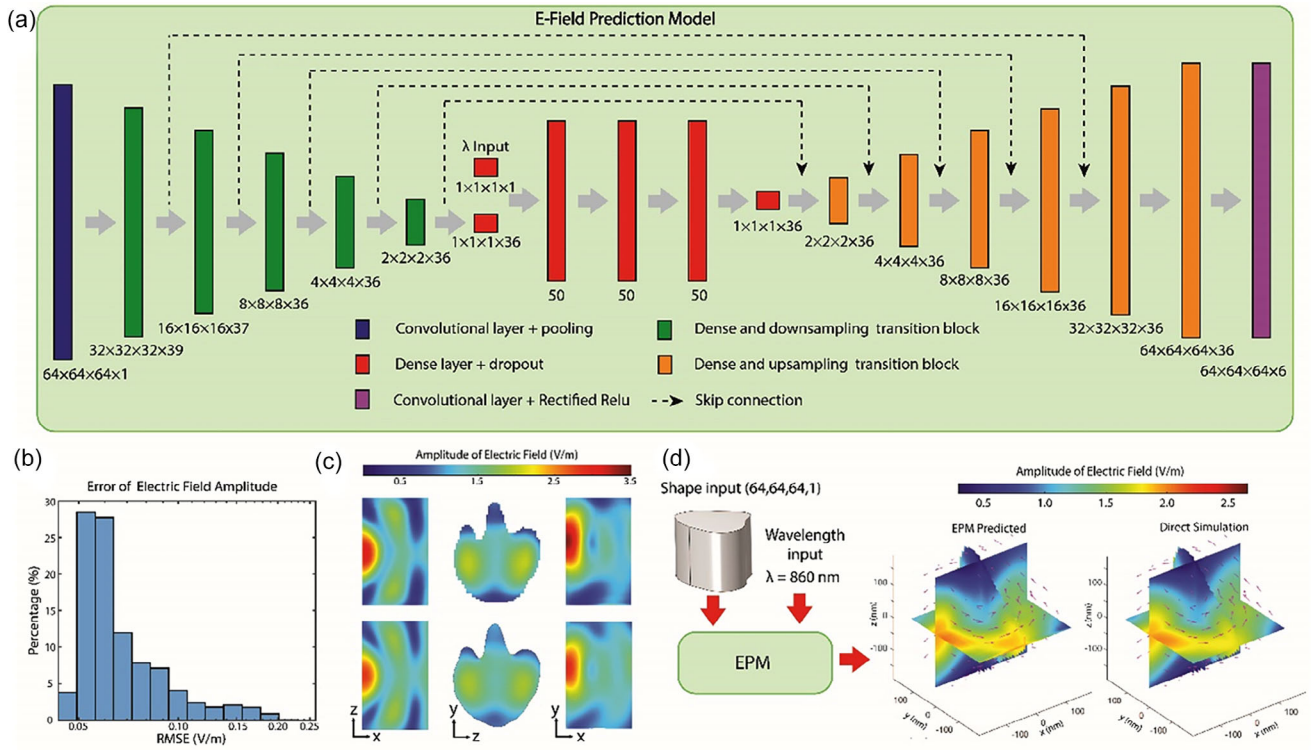

Figure 5. Electric field prediction (EPM) model for the E-field prediction. a) The schematic of the EPM for predicting the E-field distribution of the given meta-atom. The shape information is compressed into lower dimensions using multiple DCBs. The condensed information and the corresponding wavelength are then passed through three dense layers and multiple UCBs to predict the electric fields within the given meta-atom. b) The percentage of the total training dataset as a function of the calculated RMSE of the developed EPM. With only 13% of the dataset falling beyond the RMSE of 10% and an average RMSE of 7%, the developed EPM accurately predicts field distribution within the meta-atoms. c) The output of the EPM (top row) and direct simulations (bottom row) for the presented case of super-scatterer in the (x-z), (y-x), and (z-y) planes at the operating wavelength of $\lambda_{SS} = 633$ nm. The same color bar range is utilized for both cases to ensure consistent visualization and comparison between the two methods. d) A comparison between the 3D near-field distributions of another representative example obtained from the EPM and direct simulations. The arrows represent the electric field.

used the RMSE metric, as is shown in Figure 5b. In the depicted histogram plot, the *x*-axis represents the value of the RMSE, whereas the *y*-axis denotes the percentage of the whole dataset that lies within the corresponding RMSE. As can be seen from this panel, the total average error of the whole training dataset is ≈7%, while the total percentage of the dataset with RMSE above 10% is less than 13%, which indicates a good accuracy of the employed electric field prediction model. To further validate the developed EPM, we input the meta-atom geometry (Figure 4e) to our model and calculate the electric field amplitude in three distinct planes, namely (x-z), (y-x), and (z-y), at the operating wavelength of $\lambda_{SS} = 633$ nm, as shown in Figure 5c and compare the results with those obtained from direct numerical simulations (bottom row). As can be seen, the electric field distributions obtained from the EPM closely match the corresponding distributions from the direct simulations. We also tested our model on another meta-atom with a distinct geometry, shown in Figure 5d. Here, we compared the 3D electric field distributions obtained from direct simulations (left side of the panel) with those predicted by the EPM (right part of the panel). Since the results of these two approaches are in excellent agreement, while the EPM is much faster as compared to the direct numerical simulations, we conclude that the EPM might be used as a viable alternative to direct numerical simulations to design meta-atoms with desired field distribution. Additionally, the components of the electric field within the meta-atom obtained from the EPM facilitate a comprehensive analysis of the field distribution within the irregularly shaped meta-atoms (see Movies S1 and S2, Supporting Information for additional time-dependent visualizations).

2. Discussion

We have developed ML-based tools to design dielectric meta-atoms with targeted multipolar moments. By employing the FPM, IDM, and EPM, we achieved accurate prediction of the multipolar moment, retrieval of the meta-atom shapes from the specified magnitudes of the multipolar moments, and estimation of the electric field distributions in irregularly shaped meta-atoms, respectively. Specifically, the FPM was implemented to provide accurate and efficient predictions of the scattering response for meta-atoms of arbitrary shapes, eliminating the need for time-consuming numerical simulations, with high prediction accuracy as indicated by the RMSE value of $6.5 \times 10^{-4} \mu m^2$. Moreover, the IDM was employed to retrieve three representative meta-atom

Table 1. A comparative analysis of the presented study against existing literature.

Reference	Materials	Structure	Physics	FPM	IDM	EPM	Model
[43–46]	Plasmonic-Dielectric	Core–Shell	Only σ_{Tot}	×	✓	×	[43] CNN,[44] DNN,[45] MDAN, [46]TCNN
[48]	Plasmonic-Dielectric	Multilayer Cylinder	Up to σ_{MQ}	×	✓	×	Bayesian Optimization
[41]	Plasmonic and Dielectric	Arbitrary Shape	Only σ_{Tot}	×	×	✓	ResNet
[42]	Dielectric	Sphere	Only σ_{Tot}	✓	✓	×	Hybrid*
[47]	Plasmonic and Dielectric	Cube	Only σ_{Tot}	✓	×	×	GPR
This work	Dielectric	Arbitrary Shape	Up to σ_{MO}	✓	✓	✓	DenseNet & TIDM

CNN, Convolutional neural network; DNN, Deep neural network; MDAN, Modified denoising autoencoder network; TCNN, Two-channel neural networks; GPR, Gaussian process regression *Hybrid approach combines ML and genetic algorithm for inverse modeling of a single sphere scattering.

shapes optimized to support dominant magnetic octupolar response and achieve super-scattering states. We applied the developed tools to design the meta-atoms with maximized contributions of MD and MO moments at two distinct operating wavelengths, with their combined response reaching up to 61% and 50% of the total scattering response, respectively. Additionally, the designed super-scatterer demonstrated nearly a five-fold enhancement of scattering beyond the single-channel limit. The EPM was shown to accurately predict the field distribution within the given meta-atoms, allowing for the maximization of spatial mode overlap integral, which is particularly relevant in nonlinear optics.

We also note that the spectral position and type of the supported Mie resonance depend on three factors i) refractive index contrast between the meta-atom and environment, ii) geometrical shape and dimensions of the scatterer, iii) the incident wave's structural features (regular plane waves or structured light beams). Each of these parameters can affect the optical response of the meta-atom significantly and thus needs to be chosen delicately to achieve the desired response. In our study, the height of the meta-atoms that critically influence the spectral characteristics and the nature of the Mie resonances was held constant at 320 nm. This deliberate choice was made to ensure a focused investigation of the influence of other geometrical parameters and to maintain a manageable complexity within our training dataset. Given the fixed height parameter, the training dataset was explicitly designed to capture a wide range of responses up to magnetic octupole based on only one mid-index lossless material (TiO_2) and the variations in geometry. Consequently, in the inverse design methodology applied, the suggested meta-atom configuration adheres to this predefined height and material constraints when soliciting a design for a specific optical response. We acknowledge that altering the height and refractive index significantly from the current values could lead to discrepancies in the predicted optical response compared to actual behavior. Minor parameter adjustments might only result in slight spectral shifts while preserving the overall response characteristics. However, substantial changes in height or refractive index would necessitate a reevaluation of the model's predictions, as the fundamental assumptions on which the model was trained would no longer apply. It should be noted that the perceived limitations regarding the applicability of the model to such cases stem not from its inherent design but rather from the underlying physics governing light-matter interactions. In this perspective, one viable approach to address potential discrepancies and enhance the model's generality is expanding the training dataset to include the effects of varying heights and different materials on the Mie resonances. By incorporating data across a spectrum of heights and materials, the model could be trained to consider these parameters as additional parameters. This enhancement would enable the inverse design model to not only suggest the optimal geometrical shape for a desired optical response but also recommend the appropriate height and material for the meta-atoms. Such an extension would significantly improve the model's applicability to a broader range of meta-atom designs, including those with varied thicknesses or composed of high-index materials.

Table 1 provides a comprehensive comparison between the method proposed in this paper and other existing works, taking into consideration various aspects such as materials, shapes, the underlying physics involved in light-matter interactions, and the specific implemented neural networks. The presence of a cross symbol in Table 1 indicates the absence of a specific response or characteristic in the corresponding work. This comparison serves to highlight the distinct features and advantages of the method presented in this study as compared to other approaches in the field. The ML-based models developed and presented here rely on actual physical characteristics of the nanoscale resonators (meta-atoms)—their modes (multipole moments), thus offering not only a versatile tool for nanophotonic design but also an efficient technique to study the underlying physics of light-matter interactions in complex-shaped resonators in linear and nonlinear optical regimes.

We note that this work primarily explores the application of ML in Mie-Tronics, focusing on how it can be utilized to customize light-matter interactions at the nanoscale. In this perspective, our focus was not on developing novel ML methodologies, which, while potentially beneficial, was beyond the scope of our main objectives. Indeed, our primary interest was in assessing and applying existing neural network models to investigate the physics and structure of these interactions. Finally, it should be remarked that the proposed techniques can be easily applied to a wide range of nanophotonic devices and system applications, including metasurfaces and meta-waveguides.

3. Experimental Section

Numerical Simulations: The numerical simulations were carried out using the finite-element method (FEM) implemented in the commercial software COMSOL Multiphysics. In particular, the Wave Optics Module was utilized to solve Maxwell's equations in the frequency domain together with proper boundary conditions. Here, a spherical domain filled with air and a radius of 4λ was used as the background medium, while

perfectly matched layers of thickness 0.6λ were positioned outside of the background medium to act as absorbers and avoid back-scattering. The tetrahedral mesh was also chosen to ensure the accuracy of the results and allow numerical convergence. The meta-atoms were under plane wave excitation propagating along the *x*-axis with it was electric field pointing toward the *y*-axis.

Multipole Decomposition: According to the multipole expansion theory used to describe light interactions with subwavelength meta-atoms, the scattered field in the far field could be expressed as the superposition of various multipoles (up to the electric octupole term) as[9–13]

$$\boldsymbol{E}_{\mathrm{sct}}(\boldsymbol{n}) = \frac{k_0^2 \exp(ik_0 r)}{4\pi\epsilon_0 r}\left([\boldsymbol{n}\times[\boldsymbol{D}\times\boldsymbol{n}]] + \frac{1}{c}[\boldsymbol{m}\times\boldsymbol{n}] + \frac{ik_0}{6}[\boldsymbol{n}\times[\boldsymbol{n}\times\hat{Q}\boldsymbol{n}]] + \frac{ik_0}{2c}[\boldsymbol{n}\times\hat{M}\boldsymbol{n}] + \frac{k_0^2}{6}[\boldsymbol{n}\times[\boldsymbol{n}\times\hat{O}^{(e)}(\boldsymbol{nn})]] + \frac{k_0^2}{6c}[\boldsymbol{n}\times[\boldsymbol{n}\times\hat{O}^{(m)}(\boldsymbol{nn})]]\right) \quad (1)$$

where $\boldsymbol{D}$ corresponds to the exact total electric dipole (TED), $\boldsymbol{m}$ is the exact magnetic dipole (MD) moment, and $\hat{Q}$, $\hat{O}^{(e)}$, $\hat{M}$, and $\hat{O}^{(m)}$ represent the electric quadrupole (EQ), electric octupole (EO), magnetic quadrupole (MQ), and magnetic octupole (MO) tensors, respectively; $\boldsymbol{n} = \boldsymbol{r}/r$ is the unit vector directed from the meta-atom's center toward an observation point, and c and k_0 are the speed of light and wavenumber in a vacuum. Using these notations, the scattering cross-section, can be written as follows

$$\sigma_{\mathrm{Sct}} \approx \frac{k_0^4}{12\pi\epsilon_0^2\eta_0 I_0}|\boldsymbol{D}|^2 + \frac{k_0^4\mu_0}{12\pi\epsilon_0\eta_0 I_0}|\boldsymbol{m}|^2 + \frac{k_0^6}{1440\pi\epsilon_0^2\eta_0 I_0}\sum_{x_1,x_2}\left|Q_{x_1x_2}\right|^2 + \frac{k_0^6\mu_0}{160\pi\epsilon_0\eta_0 I_0}\sum_{x_1,x_2}\left|M_{x_1x_2}\right|^2 + \frac{k_0^8}{3780\pi\epsilon_0^2\eta_0 I_0}\sum_{x_1,x_2,x_3}\left|O^{(e)}_{x_1x_2x_3}\right|^2 + \frac{k_0^8\mu_0}{3780\pi\epsilon_0\eta_0 I_0}\sum_{x_1,x_2,x_3}\left|O^{(m)}_{x_1x_2x_3}\right|^2 \quad (2)$$

where I_0 corresponds to the maximum beam intensity in a focal plane, η_0, ϵ_0, and μ_0 are the impedance, permittivity, and permeability of free space, respectively, and x_1, x_2, and x_3 represent the different components of each tensor. Each of the moments in Equation (2) can be expressed in terms of the induced current within the meta-atom ($\boldsymbol{J} = \partial\boldsymbol{P}/\partial t$) as

$$\boldsymbol{D} = \frac{i}{\omega}\int j_0(k_0 r')\boldsymbol{J}(\boldsymbol{r}')\,d\boldsymbol{r}' + \frac{ik_d^2}{2\omega}\int\frac{j_2(k_d r')}{(k_d r')^2}\left[3(\boldsymbol{r}'\cdot\boldsymbol{J})\boldsymbol{r}' - r'^2\boldsymbol{J}\right]d\boldsymbol{r}' \quad (3)$$

$$\boldsymbol{m} = \frac{3}{2}\int\frac{j_1(k_d r')}{k_d r'}[\boldsymbol{r}'\times\boldsymbol{J}]\,d\boldsymbol{r}' \quad (4)$$

$$\hat{M} = 5\int\frac{j_2(k_d r')}{(k_d r')^2}\left([\boldsymbol{r}'\times\boldsymbol{J}]\otimes\boldsymbol{r}' + \boldsymbol{r}'\otimes[\boldsymbol{r}'\times\boldsymbol{J}]\right)d\boldsymbol{r}' \quad (5)$$

$$\hat{Q} = \frac{3i}{\omega}\int\frac{j_1(k_d r')}{k_d r'}\left[3(\boldsymbol{r}'\otimes\boldsymbol{J}+\boldsymbol{J}\otimes\boldsymbol{r}') - 2(r'\cdot\boldsymbol{J})\overline{\overline{I}}\right]d\boldsymbol{r}' + \frac{i6k_d^2}{\omega}\int\frac{j_3(k_d r')}{(k_d r')^3}\left[5(\boldsymbol{r}'\cdot\boldsymbol{J})\boldsymbol{r}'\otimes\boldsymbol{r}' - r'^2(\boldsymbol{J}\otimes\boldsymbol{r}'+\boldsymbol{r}'\otimes\boldsymbol{J}) - (\boldsymbol{J}\cdot\boldsymbol{r}')r'^2\overline{\overline{I}}\right]d\boldsymbol{r}' \quad (6)$$

$$\hat{O}^{(e)} = \frac{15i}{\omega}\int\frac{j_2(k_d r')}{(k_d r')^2}(\boldsymbol{J}\otimes\boldsymbol{r}'\otimes\boldsymbol{r}' + \boldsymbol{r}'\otimes\boldsymbol{J}\otimes\boldsymbol{r}' + \boldsymbol{r}'\otimes\boldsymbol{r}'\otimes\boldsymbol{J} - \hat{A})\,d\boldsymbol{r}' \quad (7)$$

$$\hat{O}^{(m)} = \frac{105}{4}\int\frac{j_3(k_d r')}{(k_d r')^3}([\boldsymbol{r}'\times\boldsymbol{J}]\otimes\boldsymbol{r}'\otimes\boldsymbol{r}' + \boldsymbol{r}'\otimes[\boldsymbol{r}'\times\boldsymbol{J}]\otimes\boldsymbol{r}' + \boldsymbol{r}'\otimes\boldsymbol{r}'\otimes[\boldsymbol{r}'\times\boldsymbol{J}] - \hat{B})\,d\boldsymbol{r}' \quad (8)$$

where $j_l(x)$ is the lth order spherical Bessel function, k_d is the wave number in the surrounding medium, $\overline{\overline{I}}$ is the 3×3 unit tensor, and the operators of $\cdot$, $\times$, and $\otimes$ represent the scalar, vector, and tensor products, respectively. It should be noted that $\hat{A}$ and $\hat{B}$ are auxiliary tensors whose components are obtained according to $A_{x_1x_2x_3} = \delta_{x_1x_2}V_{x_3} + \delta_{x_1x_3}V_{x_2} + \delta_{x_2x_3}V_{x_1}$, and $B_{x_1x_2x_3} = \delta_{x_1x_2}V'_{x_3} + \delta_{x_1x_3}V'_{x_2} + \delta_{x_2x_3}V'_{x_1}$ which $x_1 = (x, y, z)$, $x_2 = (x, y, z)$, $x_3 = (x, y, z)$ and δ is the Dirac delta while $V = 0.2[2(\boldsymbol{r}'\cdot\boldsymbol{J})\otimes\boldsymbol{r}' + r'^2\boldsymbol{J}]$ and $V' = 0.2[\boldsymbol{r}'\times\boldsymbol{J}]r'^2$.

Machine Learning (ML) Models: A forward prediction model (FPM) using Dense Convolutional Network (DenseNet) architecture was developed to predict the multipolar resonances of specific meta-atoms as functions of wavelength.[59] In particular, the meta-atom shapes were input into six down-conversion dense blocks before reaching the bottleneck layer. The FPM output comprises multipolar resonance arrays connected to the bottleneck layer through three consecutive fully connected layers. The advantage of employing DenseNet architecture lies in the fact that each layer within the model could receive inputs from all previous layers while forwarding it was feature maps to all subsequent layers. This ML process takes mere seconds, offering a significant speed advantage compared to FEM simulations. It also notes that the performance of the meta-atom design using IDM was closely tied to the variety of examples implemented in the training dataset. In particular, during the training phase, the range of the size and height of the scatterers was constrained, focusing on studying the effect of different geometric cross-sections on the induced multipolar moments within the meta-atoms. Within this framework, it was possible that the optimal meta-atom design for the targeted multipolar resonances might be achieved at sizes or heights beyond the limited range used, a scenario the current IDM was not equipped to handle directly. Nevertheless, by incorporating a broader range of meta-atom examples with diverse shapes and sizes, the training dataset could be enlarged and enhance the performance of the implemented ML models.

Supporting Information

Supporting Information is available from the Wiley Online Library or from the author.

Acknowledgements

This paper was supported in part by the National Science Foundation (NSF) (Grant No. 2240562), Office of Naval Research (ONR) (Grant No. N00014-20-1-2558), and Army Research Office Award (Grant No. W911NF2310057).

Conflict of Interest

The authors declare no conflict of interest.

Author Contributions

N.M.L. and W.L. initiated the idea of this study. W.L., H.B.S., and D.T. conducted theoretical and numerical studies. W.P.J., S.R., J.M., and N.M.L. contributed to the machine learning design and discussions. N.M.L. supervised the study performed in this work. All authors collectively contributed to the writing of the manuscript.

Data Availability Statement

The data that support the findings of this study are available from the corresponding author upon reasonable request.

Keywords

high-index nanoparticle, machine learning, Mie resonances, multipole decomposition, super scattering

Received: September 4, 2023
Revised: February 8, 2024
Published online: March 3, 2024

[1] Y. Kivshar, *Nano Lett.* **2022**, *22*, 3513.
[2] K. Koshelev, Y. Kivshar, *ACS Photonics* **2020**, *8*, 102.
[3] H. Chen, A. J. Taylor, N. Yu, *Rep. Prog. Phys.* **2016**, *79*, 076401.
[4] I. Staude, J. Schilling, *Nat. Photonics* **2017**, *11*, 274.
[5] P. Berini, *ACS Photonics* **2022**, *9*, 2204.
[6] L. Huang, S. Zhang, T. Zentgraf, *Nanophotonics* **2018**, *7*, 1169.
[7] P. Vabishchevich, Y. Kivshar, *Photon. Res.* **2023**, *11*, B50.
[8] W. Liu, Y. Kivshar, *Opt. Express* **2018**, *26*, 13085.
[9] R. Alaee, C. Rockstuhl, I. Fernandez-Corbaton, *Opt. Commun.* **2018**, *407*, 17.
[10] A. B. Evlyukhin, T. Fischer, C. Reinhardt, B. N. Chichkov, *Phys. Rev. B* **2016**, *94*, 205434.
[11] A. B. Evlyukhin, B. N. Chichkov, *Phys. Rev. B* **2019**, *100*, 125415.
[12] J. D. Jackson, *Am. J. Phys.* **1999**, *67*, 841.
[13] A. B. Evlyukhin, C. Reinhardt, B. N. Chichkov, *Phys. Rev. B* **2011**, *84*, 235429.
[14] R. Culkin, R. D. Sanjiv, *J. Invest. Manag.* **2017**, *15*, 92.
[15] M. Chua, D. Kim, J. Choi, N. G. Lee, V. Deshpande, J. Schwab, M. H. Lev, R. G. Gonzalez, M. S. Gee, S. Do, *Nat. Biomed. Eng.* **2023**, *7*, 711
[16] N. Sebe, *Machine Learning in Computer Vision*, Springer Science & Business Media, Berlin, Germany **2005**, Vol. *29*.
[17] K. Siau, W. Wang, *Cutt. Bus. Technol. J.* **2018**, *31*, 47.
[18] G. Genty, L. Salmela, J. M. Dudley, D. Brunner, A. Kokhanovskiy, S. Kobtsev, S. K. Turitsyn, *Nat. Photonics* **2021**, *15*, 91.
[19] L. Pilozzi, F. A. Farrelly, G. Marcucci, C. Conti, *Commun. Phys.* **2018**, *1*, 57.
[20] Z. A. Kudyshev, V. M. Shalaev, A. Boltasseva, *ACS Photonics* **2020**, *8*, 34.
[21] T. F. De Lima, H. T. Peng, A. N. Tait, M. A. Nahmias, H. B. Miller, B. J. Shastri, P. R. Prucnal, *J. Lightwave Technol.* **2019**, *37*, 515.
[22] Z. Liu, D. Zhu, L. Raju, W. Cai, *Adv. Sci.* **2021**, *8*, 2002923.
[23] Z. Li, R. Pestourie, Z. Lin, S. G. Johnson, F. Capasso, *ACS Photon.* **2022**, *9*, 2178.
[24] S. Krasikov, A. Tranter, A. Bogdanov, Y. Kivshar, *Opto-Electron. Adv.* **2022**, *5*, 210147.
[25] W. Ma, Z. Liu, Z. A. Kudyshev, A. Boltasseva, W. Cai, Y. Liu, *Nat. Photonics* **2021**, *15*, 77.
[26] P. R. Wiecha, A. Arbouet, C. Girard, O. L. Muskens, *Photon. Res.* **2021**, *9*, B182.
[27] O. Khatib, S. Ren, J. Malof, W. J. Padilla, *Adv. Funct. Mater.* **2021**, *31*, 2101748.
[28] K. A. Brown, S. Brittman, N. Maccaferri, D. Jariwala, U. Celano, *Nano Lett.* **2019**, *20*, 2.
[29] K. Yao, Y. Zheng, *Nanophotonics and Machine Learning: Concepts, Fundamentals, and Applications*, Springer, Springer Nature Switzerland AG, **2023**, pp. 1–178.
[30] Y. Xu, B.o Xiong, W. Ma, Y. Liu, *Prog. Quant. Electron.* **2023**, 100469.
[31] W. Ma, F. Cheng, Y. Xu, Q. Wen, Y. Liu, *Adv. Mater.* **2019**, *31*, 1901111.
[32] I. Malkiel, M. Mrejen, A. Nagler, U. Arieli, L. Wolf, H. Suchowski, *Light: Sci. Appl.* **2018**, *7*, 60.
[33] K. Yao, Y. Liu, *ACS Photonics* **2016**, *3*, 953.
[34] L. Li, H. Ruan, C. Liu, Y. Li, Y. Shuang, A. Alù, C. W. Qiu, T. J. Cui, *Nat. Commun.* **2019**, *10*, 1082.
[35] X. Shi, T. Qiu, J. Wang, X. Zhao, S. Qu, *J. Phys. D: Appl. Phys.* **2020**, *53*, 275105.
[36] W. Ma, Y. Xu, B. Xiong, L. Deng, R. W. Peng, M. Wang, Y. Liu, *Adv. Mater.* **2022**, *34*, 2110022.
[37] Z. A. Kudyshev, A. V. Kildishev, V. M. Shalaev, A. Boltasseva, *Appl. Phys. Rev.* **2020**, *7*, 021407.
[38] L. Xu, M. Rahmani, Y. Ma, D. A. Smirnova, K. Z. Kamali, F. Deng, Y. K. Chiang, L. Huang, H. Zhang, S. Gould, D. N. Neshev, *Adv. Photon.* **2020**, *2*, 026003.
[39] L. Gu, Y. He, H. Liu, Z. Wei, J. Guo, *Opt. Mater.* **2023**, *136*, 113471.
[40] S. Gladyshev, T. D. Karamanos, L. Kuhn, D. Beutel, T. Weiss, C. Rockstuhl, A. Bogdanov, "Inverse design of all-dielectric metasurfaces with bound states in the continuum," *arXiv preprint arXiv:2305.10020* **2023**.
[41] P. R. Wiecha, O. L. Muskens, *Nano Lett.* **2019**, *20*, 329.
[42] Z. Cao, F. Cui, F. Xian, C. Zhai, S. Pei, *J. Quant. Spectrosc. Radiat. Transfer* **2019**, *235*, 180.
[43] A. Vallone, N. M. Estakhri, N. M. Estakhri, *J. Phys.: Photon.* **2023**, *5*, 024002.
[44] C. Qiu, X. Wu, Z. Luo, H. Yang, G. He, B. Huang, *Opt. Express* **2021**, *29*, 28406.
[45] B. Hu, B. Wu, D. Tan, J. Xu, Y. Chen, *Opt. Express* **2019**, *27*, 36276.
[46] C. Qiu, Z. Luo, X. Wu, H. Yang, B. Huang, Inverse design of multilayer nanoparticles using artificial neural networks and genetic algorithm, *arXiv preprint arXiv:2003.08356* **2020**.
[47] E. G. Ozaktas, A. Naef, G. Tagliabue, in *2023 57th Annual Conf. on Information Sciences and Systems (CISS)*. IEEE, New York **2023**.
[48] F. Qin, D. Zhang, Z. Liu, Q. Zhang, J. Xiao, *Opt. Express* **2019**, *27*, 31075.
[49] D. Smirnova, Y. S. Kivshar, *Optica* **2016**, *3*, 1241.
[50] P. Vabishchevich, Y. Kivshar, *Photon. Res.* **2023**, *11*, B50.
[51] J. Gao, M. A. Vincenti, J. Frantz, A. Clabeau, X. Qiao, L. Feng, M. Scalora, N. M. Litchinitser, *Nat. Commun.* **2021**, *12*, 5833.
[52] J. Gao, M. A. Vincenti, J. Frantz, A. Clabeau, X. Qiao, L. Feng, M. Scalora, N. M. Litchinitser, *Nanophotonics* **2022**, *11*, 4027.
[53] D. Hähnel, C. Golla, M. Albert, T. Zentgraf, V. Myroshnychenko, J. Förstner, C. Meier, *Light: Sci. Appl.* **2023**, *12*, 97.
[54] M. A. Vincenti, J. Gao, D. de Ceglia, J. A. Frantz, M. Scalora, N. M. Litchinitser, *New J. Phys.* **2022**, *24*, 035005.
[55] M. Jin, Z. Hu, X. Liu, G. Li, *Laser Photon. Rev.* **2023**, *17*, 2300174.
[56] I. A. Al-Ani, K. As'ham, O. Klochan, H. T. Hattori, L. Huang, A. E. Miroshnichenko, *J. Opt.* **2022**, *24*, 053001.
[57] R. Verre, D. G. Baranov, B. Munkhbat, J. Cuadra, M. Käll, T. Shegai, *Nat. Nanotechnol.* **2019**, *14*, 679.

[58] H. B. Sedeh, N. M. Litchinitser, *Nanophotonics* **2023**, *12*, 2687.
[59] G. Huang, Z. Liu, L. Van Der Maaten, K. Q. Weinberger, in *Proceedings of the IEEE Conf. on Computer Vision and Pattern Recognition*, IEEE, Honolulu, HI **2017**.
[60] M. I. Jordan, D. E. Rumelhart, *Backpropagation*, Psychology Press, London **2013** 189.
[61] S. Ren, A. Mahendra, O. Khatib, Y. Deng, W. J. Padilla, J. M. Malof, *Nanoscale* **2022**, *14*, 3958.
[62] S. Ren, W. Padilla, J. Malof, *Adv. Neural. Inform. Process. Syst.* **2020**, *33*, 38.
[63] A. E. Miroshnichenko, Y. S. Kivshar, *Nano Lett.* **2012**, *12*, 6459.
[64] K. E. Chong, B. Hopkins, I. Staude, A. E. Miroshnichenko, J. Dominguez, M. Decker, D. N. Neshev, I. Brener, Y. S. Kivshar, *Small* **2014**, *10*, 1985.
[65] J. Yan, P. Liu, Z. Lin, H. Wang, H. Chen, C. Wang, G. Yang, *ACS Nano* **2015**, *9*, 2968.
[66] M. R. Shcherbakov, D. N. Neshev, B. Hopkins, A. S. Shorokhov, I. Staude, E. V. Melik-Gaykazyan, M. Decker, A. A. Ezhov, A. E. Miroshnichenko, I. Brener, A. A. Fedyanin, *Nano Lett.* **2014**, *14*, 6488.
[67] Y. G. Liu, W. C. Choy, E. I. Wei, W. C. Chew, *Opt. Lett.* **2012**, *37*, 2112.
[68] W. Liu, A. E. Miroshnichenko, D. N. Neshev, Y. S. Kivshar, *Phys. Rev. B* **2012**, *86*, 081407.
[69] Y. H. Fu, A. I. Kuznetsov, A. E. Miroshnichenko, Y. F. Yu, B. Luk'yanchuk, *Nat. Commun.* **2013**, *4*, 1527.
[70] H. B. Sedeh, D. G. Pires, N. Chandra, J. Gao, D. Tsvetkov, P. Terekhov, I. Kravchenko, N. Litchinitser, *Laser Photon. Rev.* **2023**, *17*, 2200472.
[71] M. Decker, I. Staude, I. I. Shishkin, K. B. Samusev, P. Parkinson, V. K. Sreenivasan, A. Minovich, A. E. Miroshnichenko, A. Zvyagin, C. Jagadish, D. N. Neshev, *Nat. Commun.* **2013**, *4*, 2949.
[72] S. Mühlig, A. Cunningham, S. Scheeler, C. Pacholski, T. Bürgi, C. Rockstuhl, F. Lederer, *ACS Nano* **2011**, *5*, 6586.
[73] T. Feng, Y. Xu, W. Zhang, A. E. Miroshnichenko, *Phys. Rev. Lett.* **2017**, *118*, 173901.
[74] A. Mirzaei, A. E. Miroshnichenko, I. V. Shadrivov, Y. S. Kivshar, *Appl. Phys. Lett.* **2014**, *105*, 011109.
[75] Z. Ruan, S. Fan, *Phys. Rev. Lett.* **2010**, *105*, 013901.
[76] Y. Huang, L. Gao, *J. Phys. Chem. C* **2014**, *118*, 30170.
[77] S. Lepeshov, A. Krasnok, A. Alú, *ACS Photonics* **2019**, *6*, 2126.
[78] C. Qian, X. Lin, Y. Yang, X. Xiong, H. Wang, E. Li, I. Kaminer, B. Zhang, H. Chen, *Phys. Rev. L* **2019**, *122*, 063901.
[79] W. Liu, *Phys. Rev. A* **2017**, *96*, 023854.
[80] A. C. Valero, Z. Sztranyovszky, E. A. Muljarov, A. Bogdanov, T. Weiss, *Nat. Commun.* **2023**, *14*, 4689.
[81] A. V. Kuznetsov, A. C. Valero, H. K Shamkhi, P. Terekhov, X. Ni, V. Bobrovs, M. V. Rybin, A. S. Shalin, *Sci. Rep.* **2022**, *12*, 21904.
[82] A. Mirzaei, I. V. Shadrivov, A. E. Miroshnichenko, Y. S. Kivshar, *Opt. Express* **2013**, *21*, 10454.
[83] S. H. Raad, C. J. Zapata-Rodríguez, Z. Atlasbaf, *JOSA B* **2019**, *36*, 2292.
[84] R. Li, B. Zheng, X. Lin, R. Hao, S. Lin, W. Yin, E. Li, H. Chen, *IEEE J. Sel. Top. Quant. Electron.* **2016**, *23*, 130.
[85] V. I. Shcherbinin, V. I. Fesenko, T. I. Tkachova, V. R. Tuz, *Phys. Rev. Appl.* **2020**, *13*, 024081.
[86] C. A. Balanis, *Antenna Theory: Analysis and Design*, John Wiley & Sons, Hoboken, NJ **2016**.
[87] C. Gigli, T. Wu, G. Marino, A. Borne, G. Leo, P. Lalanne, *ACS Photonics* **2020**, *7*, 1197.